ADVANCED MATERIALS
www.advmat.de

A Thermal Radiation Modulation Platform by Emissivity Engineering with Graded Metal–Insulator Transition

*Kechao Tang, Xi Wang, Kaichen Dong, Ying Li, Jiachen Li, Bo Sun, Xiang Zhang, Chris Dames, Chengwei Qiu, Jie Yao, and Junqiao Wu**

Thermal radiation from a black body increases with the fourth power of absolute temperature (T^4), an effect known as the Stefan–Boltzmann law. Typical materials radiate heat at a portion of this limit, where the portion, called integrated emissivity (ε_{int}), is insensitive to temperature ($|d\varepsilon_{int}/dT| \approx 10^{-4}$ °C^{-1}). The resultant radiance bound by the T^4 law limits the ability to regulate radiative heat. Here, an unusual material platform is shown in which ε_{int} can be engineered to decrease in an arbitrary manner near room temperature ($|d\varepsilon_{int}/dT| \approx 8 \times 10^{-3}$ °C^{-1}), enabling unprecedented manipulation of infrared radiation. As an example, ε_{int} is programmed to vary with temperature as the inverse of T^4, precisely counteracting the T^4 dependence; hence, thermal radiance from the surface becomes temperature-independent, allowing the fabrication of flexible and power-free infrared camouflage with unique advantage in performance stability. The structure is based on thin films of tungsten-doped vanadium dioxide where the tungsten fraction is judiciously graded across a thickness less than the skin depth of electromagnetic screening.

As a strongly correlated electron material, vanadium dioxide (VO_2) features a well-known, temperature-driven metal–insulator phase transition (MIT) at $T_{MIT} = 67$ °C.[1–3] It takes the insulating (I) phase at $T < T_{MIT}$ and abruptly switches to the metallic (M) phase at $T > T_{MIT}$. In the thermal IR spectral range near room temperature (wavelength between ≈5 and ≈20 µm), the M phase of VO_2 is much more reflective than the I phase, because its plasma energy of free electrons is ≈1 eV,[4,5] significantly higher than that of the thermal IR photons (≈ 0.1 eV). Therefore, much less IR energy is absorbed when VO_2 undergoes the phase transition and becomes metallic.[6–9] According to the Kirchhoff's law of radiation,[10] the spectral emissivity, $\varepsilon(\lambda)$, is equal to absorptivity in the IR regime. When averaged for thermal radiation, an abrupt drop[11] in the integrated emissivity (ε_{int}) and hence thermal radiance is thus expected for VO_2 at $T = T_{MIT}$, as schematically illustrated in **Figure 1**a, and experimentally measured and shown in Figure S1, Supporting Information. Here, the thermal radiance per unit solid angle is given by[12]

$$P_{rad}(T) = \int_0^\infty B(T,\lambda)\varepsilon(\lambda)d\lambda \quad (1)$$

where $B(T,\lambda) = \frac{2hc^2}{\lambda^5}\frac{1}{e^{hc/(\lambda k_B T)} - 1}$ is the spectral radiance of a black body, k_B is the Boltzmann constant, h is the Planck

Dr. K. Tang, Dr. X. Wang,[+] Dr. K. Dong, J. Li, Prof. J. Yao, Prof. J. Wu
Department of Materials Science and Engineering
University of California
Berkeley, CA 94720, USA
E-mail: wuj@berkeley.edu
Dr. K. Tang, Prof. X. Zhang, Prof. J. Yao, Prof. J. Wu
Division of Materials Sciences
Lawrence Berkeley National Laboratory
Berkeley, CA 94720, USA
Dr. Y. Li, Prof. C. Qiu
Department of Electrical and Computer Engineering
National University of Singapore
Singapore 117583, Singapore
Prof. B. Sun
Tsinghua-Berkeley Shenzhen Institute
Tsinghua University
Shenzhen 518055, China
Prof. X. Zhang
NSF Nanoscale Science and Engineering Center (NSEC)
University of California
Berkeley, CA 94720, USA
Prof. X. Zhang
University of Hong Kong
Hong Kong, China
Prof. C. Dames
Department of Mechanical Engineering
University of California
Berkeley, CA 94720, USA

The ORCID identification number(s) for the author(s) of this article can be found under https://doi.org/10.1002/adma.201907071.

[+]Present address: Department of Materials Science and Engineering, University of Delaware, Newark, DE 19716, USA

DOI: 10.1002/adma.201907071

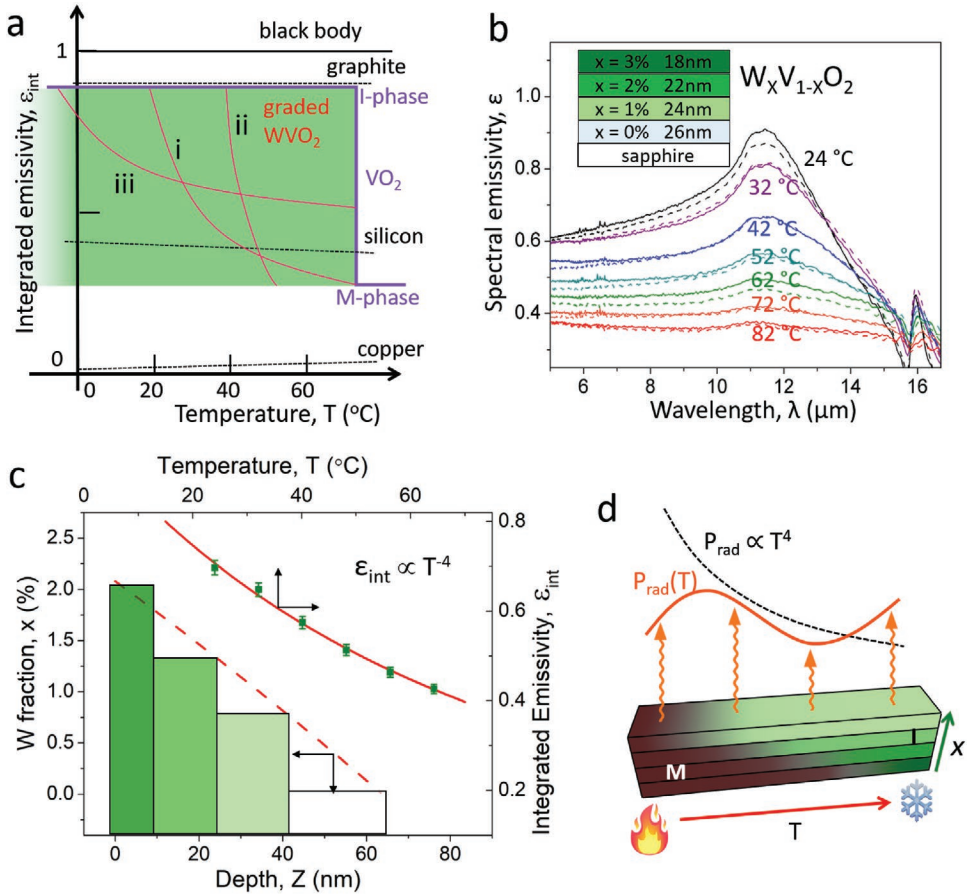

Figure 1. Engineering thermal IR emissivity by grading metal (M)–insulator (I) transition. a) Schematic illustrating realization of nearly arbitrary temperature dependence of integrated emissivity (ε_{int}) within the shaded area using graded W-doped VO_2, represented by the three arbitrarily designed emissivity curves denoted by i, ii, and iii. The behavior of typical high, moderate, and low-ε_{int} materials and of VO_2 is also shown for comparison. b) Spectral emissivity of a graded $W_xV_{1-x}O_2$ structure (schematic in inset) measured over a broad range of temperature, showing a smoothly but rapidly reduced ε_{int}. The solid and dashed curves correspond to data collected during heating and cooling, respectively. The spectral behavior in the long-wavelength region is related to the substrate (Figures S1 and S11, Supporting Information). c) Design of W doping profile $x(Z)$ (dashed line, left-bottom axes) to generate the desired $\varepsilon_{int}(T)$ relation (solid line, right-up axes). The boxes represent actual nominal doping profile used in the WVO_2 film deposition, and the data points are the experimentally measured $\varepsilon_{int}(T)$ from this film, which agrees well with the desired $\varepsilon_{int}(T)$. d) Schematic showing that by rational design of the W doping profile (x along thickness direction) of $W_xV_{1-x}O_2$, emissivity can be programed to regulate thermal radiation (P_{rad}) for distinctly different behavior from the Stefan–Boltzmann T^4 law.

constant, c is the speed of light, λ is the wavelength, and $\varepsilon(\lambda)$ is the spectral emissivity. Conveniently, T_{MIT} of VO_2 can be rapidly shifted from 67 °C to lower temperatures, down to temperatures beyond –100 °C, by doping with tungsten (W) to form $W_xV_{1-x}O_2$ alloys.[13–15] The reduction of T_{MIT} follows a rate of $dT_{MIT}(x)/dx \approx -25$ °C per at% as measured in our films and shown in Figure S2, Supporting Information. The contrasts in both electrical resistivity and ε_{int} between the I and M phases are largely retained for low-fraction W doping. However, the abrupt nature of MIT in $W_xV_{1-x}O_2$ at those T_{MIT} values limits any application of the MIT to be within a narrow temperature window around T_{MIT}. This window is typically narrower than ≈20 °C (Figure S2, Supporting Information), and outside this window, the material would behave as either a regular insulator (in the I phase) or a regular metal (in the M phase).

To overcome this limit, we designed and deposited multilayer $W_xV_{1-x}O_2$ films with total thickness less than ≈100 nm, as schematically shown in the inset of Figure 1b. Interlayer diffusion of W took place during the film deposition and post-deposition annealing. As a result, the multilayer structure becomes a graded W-doped VO_2 film, where x varies continuously across the thickness direction (Figures S2 and S3, Supporting Information). Indeed, the lack of kinks and abrupt changes in the electrical sheet resistance of the multilayer indicate that it becomes a smoothly graded W-doped structure. The graded doping spreads out the MIT from the original narrow temperature window near T_{MIT} to a broad temperature range spanning from $T_{MIT}(x_{max})$ to $T_{MIT}(x_{min})$. The drop in emissivity between the I and M phases becomes no longer abrupt and is also extended to this temperature range. We note that it is critical to grade the MIT within a thickness less than the skin depth (≈130 nm) of electromagnetic screening in the M-phase, so that the emissivity for surface radiation can be modulated by the MIT progressing away from the film surface (details in Supporting Information). The temperature dependence of $\varepsilon(\lambda)$ of a representative graded WVO_2 film was measured

using Fourier transform IR (FTIR) spectroscopy and is shown in Figure 1b. The spectral emissivity is integrated with $B(T, \lambda)$ over the atmospheric transparency window (8–14 μm) and divided by the black body integration between the same wavelength limits to obtain $\varepsilon_{int}(T)$. The large reduction in ε_{int} from ≈0.75 to ≈0.35 over a temperature range of ≈50 °C (schematic curve i in the shaded area in Figure 1a), at a rate of $d\varepsilon_{int}/dT \approx -8 \times 10^{-3}$ °C^{-1}, is orders of magnitude stronger than that of conventional materials. For example, as schematically shown in Figure 1a, $d\varepsilon_{int}/dT$ near room temperature is about 2×10^{-5} °C^{-1} for graphite (a high-ε_{int} material),[16] -1×10^{-4} °C^{-1} for silicon (a moderate-ε_{int} material),[17] and 1×10^{-4} °C^{-1} for typical metals (low-ε_{int} materials).[18] This temperature insensitivity of ε_{int} in conventional materials arises fundamentally from the fact that temperature variation is a small perturbation in energy with respect to typical radiative electronic and phononic processes in solids.[19] The W doping profile can be designed to be more tightly distributed across the structure to achieve even greater $|d\varepsilon_{int}/dT|$ (curve ii in Figure 1a), but at the cost of a narrower working temperature range. An example of designing the W doping profile to successfully create the desired $\varepsilon_{int}(T)$ is shown in Figure 1c (details in Supporting Information). Therefore, this structure provides a platform where emissivity can be engineered to exhibit nearly arbitrary, strong temperature dependence beyond that of conventional materials. Following the Stefan–Boltzmann law, the thermal radiance from the surface would be regulated to have temperature dependences distinctly different from the conventional T^4 law, as depicted in Figure 1d. Exploiting the ε_{int}-regulated thermal radiation, we demonstrate a mechanically flexible and power-free thermal IR camouflage as well as a thermal IR decoy, both inherently robust and immune to drastic temporal fluctuation and spatial variation of temperature.

As the first example, we demonstrate a thermal IR camouflage using the graded WVO_2 platform, of which the working principle is shown in **Figure 2**a. When x and thickness of each layer were judiciously selected (Figure 1c), the graded doped WVO_2 exhibits an ε_{int} that depends on temperature following $\approx 1/T^4$. The FTIR-measured $\varepsilon_{int}(T)$ of a sample prepared following this design method (details in Figure S4, Supporting Information) is shown in Figure 2b. The $1/T^4$ dependence of $\varepsilon_{int}(T)$ is multiplied with the Stefan–Boltzmann T^4 relation of a black body, to give the T-independent thermal radiance P_{rad}, as shown in Figure 2b. The constant P_{rad} over a temperature range over 50 °C near room temperature invalidates the assumption of T-dependent P_{rad}, the principle behind IR imaging.[20,21] As such, the structure would appear to have a constant IR temperature (T_{IR}) when imaged by an IR camera, despite the reality that its actual temperature (T_{actual}) may vary widely. Unlike low-emissivity camouflage coatings that rely on reflection signals from a confinement and thus limited to indoor scenarios, the IR camouflage based on graded WVO_2 fools the camera by manipulating thermal radiation from the target itself, making it ideal for outdoor applications.

Existing IR camouflage techniques use a coating whose emissivity can be modulated by effects of thermochromics,[22–24] electrochromics,[25–28] photocarrier doping,[29] or mechanical actuation.[30] These active camouflage techniques generally require energy input to operate, and are based on rigid and complicated heterostructures. They are also typically limited to only camouflage objects with uniform and slow-varying temperature profiles. In contrast, our graded WVO_2 offers an IR camouflage that is power-free, monolithic, and mechanically flexible. A detailed comparison of key capabilities and figures of merits with existing IR camouflage systems can be found in Table S3, Supporting Information. Using a wet etch-transfer method (see Experimental Section; Figure S5, Supporting Information), the graded WVO_2 film is transferred from the growth substrate onto a polyethylene (PE) tape. As the total thickness of the WVO_2 film is less than 100 nm, the WVO_2/tape structure can be bent to curvatures exceeding 10 cm^{-1} (Figure 2c) without degrading its camouflage performance. The mechanical flexibility combined with the angular-independence of emissivity (Figure S6, Supporting Information) allows the camouflage to be easily applied as a tape onto non-flat surfaces, with minimal or no impact to the performance (Figure S7, Supporting Information). No noticeable degradation in camouflage property or change in surface morphology was detected after up to 100 heating/cooling cycles through the working temperature range (15–65 °C), demonstrating good reliability of the film (Figure S8, Supporting Information). In Figure S8, Supporting Information, a T_{IR} difference of ≈3 °C is observed between the heating and cooling branches, caused by the hysteresis effect of the WVO_2 phase transition. This degree of impact should not affect the general applicability of the technique, and could be reduced by future work to optimize the hysteresis, including process by crystal dehydration[31] or Ti doping method.[32]

A series of experiments were conducted to test the performance of the camouflage. Figure 2c shows optical image and IR snapshot of a finger where the tip is covered by the camouflage. Distinct from the exposed skin, the part covered by the camouflage displays a T_{IR} similar to the environment, concealing the fingertip from IR detection. Apart from such conventional application as a living body camouflage, our structure has the inherent, unique advantage to cover up objects with large spatial variation (∇T) or abrupt temporal fluctuation (dT/dt) of temperature. In Figure 2d, a copper plate coated with high-emissivity tape is thermally biased with T_{actual} varying from 25 to 65 °C. Three identical WVO_2 camouflages were placed at different positions of the plate that have distinct local temperatures. The regions underneath the camouflages are simultaneously masked from IR detection regardless of the different local temperatures and high thermal gradient. Compared to using multiplexing to address the spatial temperature variation in conventional camouflages,[26,29] the graded WVO_2 design offers a much simpler, monolithic, power-free, and tetherless approach.

The camouflage is also inherently immune against abrupt temperature fluctuation. In Figure 2e, a heater membrane is partly covered by our graded WVO_2 film transferred onto a high-emissivity PE tape (sample), and the rest is covered by the high-emissivity PE tape alone (control). The temperature of the plate shoots up rapidly when a current pulse passes through the heater. The IR camera catches clearly a temperature spiking up to 65 °C within less than 2 s from the control surface, while the camouflaged surface stays at nearly constant T_{IR} of 20 °C irrespective of the heat pulse (see Video S1, Supporting Information). The detected T_{IR} is plotted as a function of time in

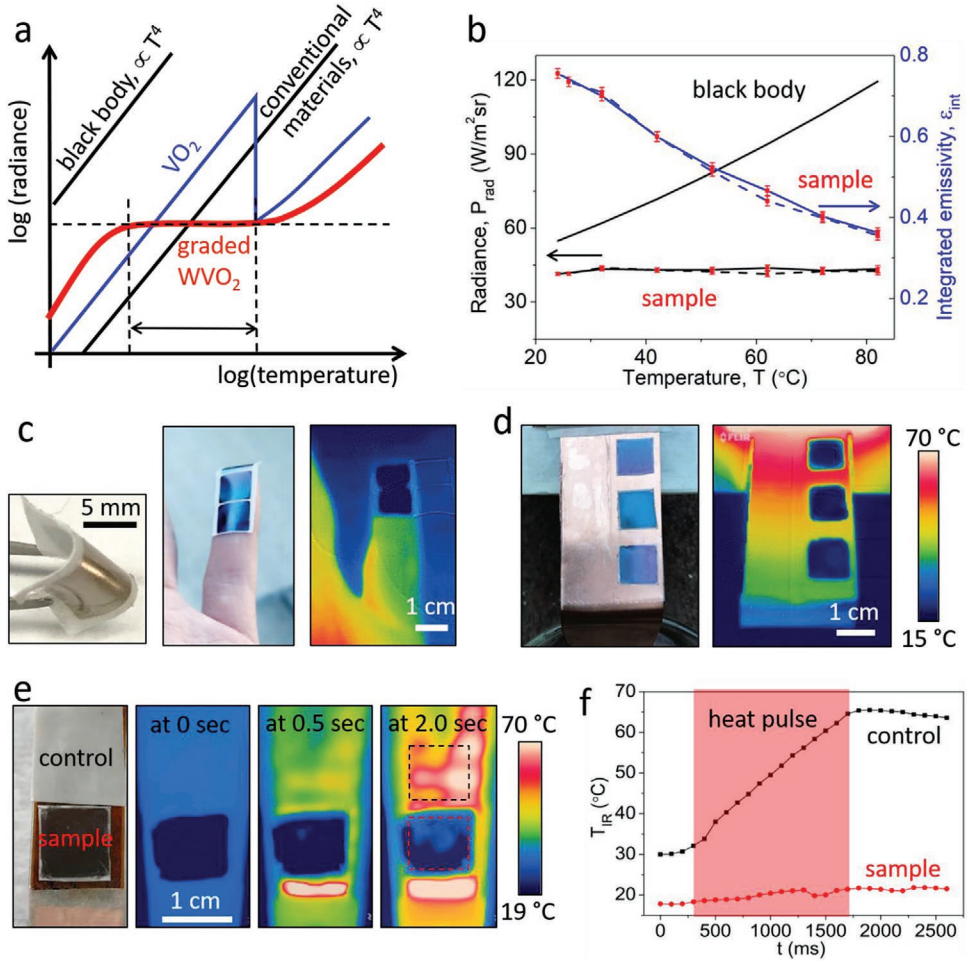

Figure 2. Mechanically flexible, power-free, and ∇T- and dT/dt-immune camouflage based on the graded WVO_2. a) Schematic illustrating constant thermal radiance over a wide range of temperature from the camouflage, in stark contrast to the Stefan–Boltzmann T^4 law from conventional materials. b) Thermal radiance and integrated emissivity of the film as a function of temperature, showing that the negative temperature coefficient of emissivity counteracts the T^4 law to yield a temperature-independent thermal radiation power. The solid and dashed curves are for measurements during heating and cooling, respectively. c) Optical image of a graded WVO_2 film transferred onto a PE tape showing high mechanical flexibility. The visible color of the sample is related to the WVO_2 thickness and lighting on surface (see Experimental Section). The fingertip is hidden from the IR camera when covered with the camouflage. d) Camouflaging an object with large spatial temperature variation from ≈25 to 65 °C, showing immunity to ∇T. e) Camouflaging an object with drastic temperature surge, showing immunity to dT/dt. As shown in (f), the actual temperature of the camouflage (represented by the IR temperature of the control that is a high-emissivity tape placed near the sample) rises rapidly by the heating pulse, while the IR temperature of the camouflage stays nearly flat. The IR temperature was measured by averaging the camera reading in the center 1×1 cm^2 region of each film (dashed boxes), and the error bars are comparable to the symbols in size.

Figure 2f, which shows a nearly total immunity to the temperature surge. This immunity is a substantial advantage over the strategy of adjusting the emissivity using a feedback loop in conventional camouflages, as the latter typically has a response time over seconds[26,27,30] and would have the object exposed to detection during the response lagging time.

Next, we demonstrate another unique function, a thermal IR "decoy," using the structure. A decoy is different from the camouflage in the way that the decoy would not only passively conceal the real thermal activity of the object from an IR camera, but also intentionally fool the camera with a counterfeited T_{IR} image that is independent of T_{actual} distribution and fluctuation. That is, to create a robust thermal radiative pattern $T_{IR}(X,Y,Z)$ on a surface that has arbitrary actual temperature distribution $T_{actual}(X,Y,Z,t)$, where X, Y, and Z are the coordinates of the surface and t is time. Because the overall emissivity of the graded WVO_2/tape system is the combined effect of both the WVO_2 film and the tape, by using different doping profiles for the graded WVO_2 film and transferring onto different tapes, T_{IR} of the camouflage can be designed to take distinct values to meet different requirements. A series of flexible WVO_2/tape samples were prepared (details in Figure S9, Supporting Information). As shown in **Figure 3**a, despite T_{actual} varying widely from room temperature to ≈70 °C, these samples all exhibit a nearly constant T_{IR} within the T_{actual} range, whereas T_{IR} is designed to be equal to any desired value in the range of 5–30 °C. As a proof of concept, Figure 3b,c demonstrates a working decoy where the image of "CAL" shows a stable IR

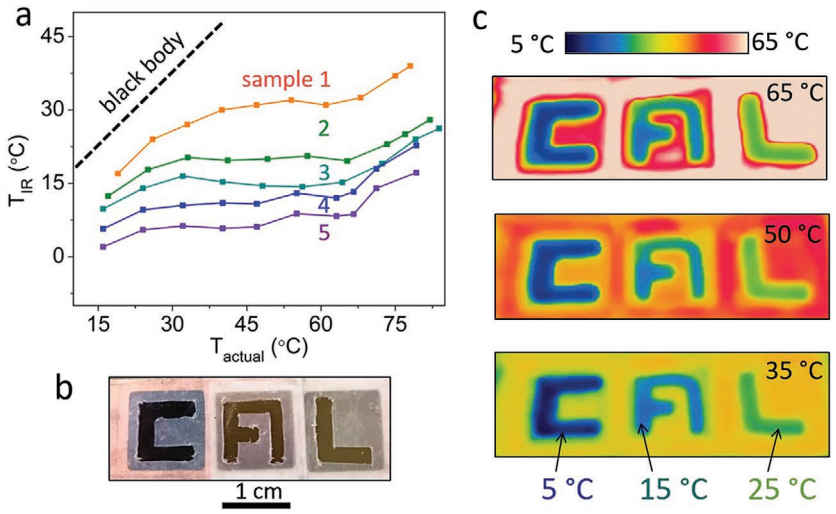

Figure 3. Demonstration of T_{actual}-independent thermal IR decoy. a) IR temperature (T_{IR}) versus actual temperature (T_{actual}) of five flexible structures, where the graded WVO_2 configuration is designed to yield T_{actual}-independent, but different, values of desired T_{IR} within the working range of T_{actual}. Details of these samples are shown in Figure S9, Supporting Information. The error bars are comparable to the symbols in size. b) Optical and c) IR images, using the samples 1, 3, and 5, respectively. A pattern of "CAL" is made to show "C" at constant $T_{IR} \approx 5$ °C, "A" at $T_{IR} \approx 15$ °C, and "L" at $T_{IR} \approx 25$ °C, regardless of T_{actual} varying to 65, 50, or 35 °C. The three samples are all 1×1 cm^2 in size.

temperature reading, regardless of the change in T_{actual}. Such decoying information can be also encoded during the film deposition by laterally patterning the composition and thickness of the graded WVO_2 film, allowing fabrication of a monolithic and lithographically manufacturable decoy (Figure S10, Supporting Information).

While these features greatly expand the application of radiative camouflage to inhomogeneous and dynamic environments as well as IR decoying, they also inspire novel device concepts based on reflection or transmission of IR signals. As expected, over the broad spectral range from near-IR (down to the plasma wavelength ≈1.2 µm) to the far-IR, the reflectivity of the graded WVO_2 would exhibit a temperature dependence that is much stronger than that of conventional materials (Figure S11, Supporting Information, shows part of the spectrum). This feature enables potential ways for high-sensitivity remote temperature sensing using thermoreflectance imaging, or active reflectance modulation of IR signals. Therefore, the graded WVO_2 structure offers a general platform for unprecedented manipulation and processing of IR signals for novel radiative and reflective systems.

Experimental Section

Thin Film Deposition and Etching/Transfer Process: WVO_2 thin films were grown on c-cut sapphire and borosilicate glass substrates using pulsed laser deposition (PLD). The graded W doping was achieved by sequentially focusing the pulsed laser on a series of WVO_2 targets with different W doping ratios. The targets were prepared by mixing WO_3 and V_2O_5 powders with W/V the atomic ratio ranging from 0% to 3.0%, then made into 1 in. diameter round discs with a hydraulic press. All thin films were deposited in 5 mTorr O_2 environment at 475 °C substrate temperature. The PLD laser energy was set at 321 mJ with 5 Hz pulse frequency. A post-deposition anneal at 475 °C for 30 min in the same 5 mTorr O_2 environment was performed for all graded doped WVO_2 film. The thickness and deposition rate of the thin films were measured by atomic force microscopy and scanning electron microscopy (Figure S12, Supporting Information), and the W faction as well as depth profile was characterized by X-ray photoelectron spectroscopy (Figure S3, Supporting Information).

WVO_2 thin films grown on borosilicate glass substrates were transferred onto PE tapes by sticking the WVO_2 side to the adhesive side of the tape, and then etching off the 170 µm thick substrate by dipping into 49% hydrofluoric acid for 5 min. The samples with transferred WVO_2 were then rinsed in deionized water for 3 min and gently blown dry with a N_2 gun. The interfacial adhesion was strong and no delamination of WVO_2 was observed during the wet transfer process, in further contact with water, or with mechanical bending and twisting of the tape. The thickness of the PE tape (default) and the scotch tape was ≈0.20 and 0.08 mm, respectively. The visible color mainly depends on the thickness of the graded WVO_2 coating layer. Thicker film will appear blue/purple, while thinner film tends to have brown/yellow color. When taking a photo, the lighting and the reflection will affect the visible appearance of the sample surface as well.

FTIR Measurements and IR Imaging: The normal-direction emissivity $\varepsilon(\lambda,T)$ was obtained from normal-incident reflection measurements following the equation: $\varepsilon(\lambda,T) = 1 - R(\lambda,T)$, due to negligible transmission $T(\lambda,T)$ of the sample over the spectra of interest. The reflection spectra, $R(\lambda,T)$, were characterized by an Agilent Cary 670 FTIR spectrometer and Agilent Cary 620 microscope system with a 15× objective lens (numerical aperture of 0.62). A blade aperture of 60 µm × 60 µm was used to select the area of interest. For measurements of samples on PE tapes, flat regions away from substrate curving spots were chosen to minimize scattering, and multiple (>3) measurements were performed to confirm repeatability of the results. All reflection spectra were normalized to the reflection spectrum of a 300 nm thick gold film. The temperature of the samples was controlled by a customized closed-loop thermal stage, connected to a Lakeshore 321 temperature controller.

The IR images and videos were captured by a FLIR ONE infrared camera. To avoid reflection signals from the camera and the surrounding, the default viewing angle was set as 15° instead of normal incident direction, and the experiments were performed in an open-area outdoor environment under clear sky (little cloud). The temperature was controlled by the same thermal stage used in the FTIR measurements. When taking an IR image, the camera measures the incident thermal radiation P_{rad}, and gives the temperature reading (T_{IR}) assuming a constant emissivity for the target ($\varepsilon_0 = 0.90$). The relationship can be described by the equation: $\varepsilon_0 \sigma T_{IR}^4 = P_{rad}$. The T_{IR} was then plotted as a function of actual temperature (T_{actual}) to demonstrate the camouflage performance.

The error bars for data presented in this work are based on standard deviation of at least three separate samples. This applies to both the figures in the manuscript and the supporting information.

Supporting Information

Supporting Information is available from the Wiley Online Library or from the author.

Acknowledgements

This work was supported by the U.S. NSF grant number DMR-1608899. The materials preparation part was done at the Electronic Materials Program at the Lawrence Berkeley National Laboratory supported by Director, Office of Science, Office of Basic Energy Sciences, Materials Sciences and Engineering Division, of the U.S. Department of Energy under contract number DE-AC02-05CH11231. K.T. acknowledges the Bakar Spark Funds. X.W. and J.Y. acknowledge support from the U.S. National Science Foundation under grant number 1555336. C.Q. acknowledges support from the A*STAR Pharos Program (grant no. 1527000014, with project no. R-263- 000-B91-305). The authors thank Prof. Peter Fan Yang for helpful discussion.

Conflict of Interest

The authors declare no conflict of interest.

Author Contributions

J.W. conceived the project. J.W. and K.T. designed the experiments. K.T. prepared the materials, fabricated the devices, and performed the measurements. X.W. helped with training and measurements of the FTIR. X.Z. provided instrumental support for the FTIR experiments. K.D. performed theoretical modeling. J.L. helped with preparation of the figures and SEM measurement. All authors contributed to discussing the data and editing the manuscript.

Keywords

emissivity engineering, infrared camouflage, materials platforms, metal–insulator transition, thermal radiation

Received: October 29, 2019
Revised: January 29, 2020
Published online: July 23, 2020

[1] F. J. Morin, *Phys. Rev. Lett.* **1959**, *3*, 34.
[2] J. Jian, X. Wang, L. Li, M. Fan, W. Zhang, J. Huang, Z. Qi, H. Wang, *ACS Appl. Mater. Interfaces* **2017**, *9*, 5319.
[3] F. Ligmajer, L. Kejík, U. Tiwari, M. Qiu, J. Nag, M. Konečný, T. Šikola, W. Jin, R. F. Haglund, K. Appavoo, D. Y. Lei, *ACS Photonics* **2018**, *5*, 2561.
[4] M. M. Qazilbash, M. Brehm, B.-G. Chae, P.-C. Ho, G. O. Andreev, B.-J. Kim, S. J. Yun, A. V. Balatsky, M. B. Maple, F. Keilmann, H.-T. Kim, D. N. Basov, *Science* **2007**, *318*, 1750.
[5] V. Eyert, *Phys. Rev. Lett.* **2011**, *107*, 016401.
[6] A. S. Barker, H. W. Verleur, H. J. Guggenheim, *Phys. Rev. Lett.* **1966**, *17*, 1286.
[7] T. Ben-Messaoud, G. Landry, J. P. Gariépy, B. Ramamoorthy, P. V. Ashrit, A. Haché, *Opt. Commun.* **2008**, *281*, 6024.
[8] M. A. Kats, R. Blanchard, S. Zhang, P. Genevet, C. Ko, S. Ramanathan, F. Capasso, *Phys. Rev. X* **2013**, *3*, 041004.
[9] S. Wang, G. Liu, P. Hu, Y. Zhou, Y. Ke, C. Li, J. Chen, T. Cao, Y. Long, *Adv. Mater. Interfaces* **2018**, *5*, 1801063.
[10] J. Agassi, *Science* **1967**, *156*, 30.
[11] K. Ito, K. Nishikawa, H. Iizuka, H. Toshiyoshi, *Appl. Phys. Lett.* **2014**, *105*, 253503.
[12] R. W. Boyd, *Radiometry and the Detection of Optical Radiation*, Wiley, New York **1983**.
[13] D. Liu, H. Cheng, X. Xing, C. Zhang, W. Zheng, *Infrared Phys. Technol.* **2016**, *77*, 339.
[14] Z. Mao, W. Wang, Y. Liu, L. Zhang, H. Xu, Y. Zhong, *Thin Solid Films* **2014**, *558*, 208.
[15] S. Lee, K. Hippalgaonkar, F. Yang, J. Hong, C. Ko, J. Suh, K. Liu, K. Wang, J. J. Urban, X. Zhang, C. Dames, S. A. Hartnoll, O. Delaire, J. Wu, *Science* **2017**, *355*, 371.
[16] R. J. Thorn, O. C. Simpson, *J. Appl. Phys.* **1953**, *24*, 633.
[17] T. Satō, *Jpn. J. Appl. Phys.* **1967**, *6*, 339.
[18] A. H. Sully, E. A. Brandes, R. B. Waterhouse, *Br. J. Appl. Phys.* **1952**, *3*, 97.
[19] M. F. Modest, *Radiative Heat Transfer*, Elsevier Science, San Diego, CA, USA **2013**.
[20] E. H. Putley, *Phys. Technol.* **1973**, *4*, 202.
[21] C. D. Tran, *Anal. Lett.* **2005**, *38*, 735.
[22] X. Liu, W. J. Padilla, *Adv. Mater.* **2016**, *28*, 871.
[23] L. Xiao, H. Ma, J. Liu, W. Zhao, Y. Jia, Q. Zhao, K. Liu, Y. Wu, Y. Wei, S. Fan, K. Jiang, *Nano Lett.* **2015**, *15*, 8365.
[24] H. Ji, D. Liu, H. Cheng, C. Zhang, L. Yang, D. Ren, *RSC Adv.* **2017**, *7*, 5189.
[25] P. Chandrasekhar, B. J. Zay, G. C. Birur, S. Rawal, E. A. Pierson, L. Kauder, T. Swanson, *Adv. Funct. Mater.* **2002**, *12*, 95.
[26] O. Salihoglu, H. B. Uzlu, O. Yakar, S. Aas, O. Balci, N. Kakenov, S. Balci, S. Olcum, S. Süzer, C. Kocabas, *Nano Lett.* **2018**, *18*, 4541.
[27] B. Kim, J. K. Koh, J. Park, C. Ahn, J. Ahn, J. H. Kim, S. Jeon, *Nano Convergence* **2015**, *2*, 19.
[28] J. Park, J.-H. Kang, X. Liu, S. J. Maddox, K. Tang, P. C. McIntyre, S. R. Bank, M. L. Brongersma, *Sci. Adv.* **2018**, *4*, eaat3163.
[29] Z. J. Coppens, J. G. Valentine, *Adv. Mater.* **2017**, *29*, 1701275.
[30] C. Xu, G. T. Stiubianu, A. A. Gorodetsky, *Science* **2018**, *359*, 1495.
[31] X. Li, L. Yang, S. Zhang, X. Li, J. Chen, C. Huang, *Mater. Lett.* **2018**, *211*, 308.
[32] S. Chen, J. Liu, L. Wang, H. Luo, Y. Gao, *J. Phys. Chem. C* **2014**, *118*, 18938.